Complex suppression patterns distinguish between major energy loss effects in Quark-Gluon Plasma

Magdalena Djordjevic[1]

[1] *Institute of Physics Belgrade, University of Belgrade, Serbia*

Interactions of high momentum partons with Quark-Gluon Plasma created in relativistic heavy-ion collisions provide an excellent tomography tool for this new form of matter. Recent measurements for charged hadrons and unidentified jets at the LHC show an unexpected flattening of the suppression curves at high momentum, exhibited when either momentum or the collision centrality is changed. Furthermore, a limited data available for B probes indicate a qualitatively different pattern, as nearly the same flattening is exhibited for the curves corresponding to two opposite momentum ranges. We here show that the experimentally measured suppression curves are well reproduced by our theoretical predictions, and that the complex suppression patterns are due to an interplay of collisional, radiative energy loss and the dead-cone effect. Furthermore, for B mesons, we predict that the uniform flattening of the suppression indicated by the limited dataset is in fact valid across the entire span of the momentum ranges, which will be tested by the upcoming experiments. Overall, the study presented here, provides a rare opportunity for pQCD theory to qualitatively distinguish between the major energy loss mechanisms at the same (nonintuitive) dataset.

arXiv:1512.00505v1 [nucl-th] 1 Dec 2015

Introduction. In the collisions of ultra-relativistic heavy ions at RHIC and LHC experiments, a new state of matter, called Quark-Gluon Plasma (QGP), is created. Rare high momentum probes transverse and interact with the medium, providing an excellent QGP tomography tool [1]. Utilizing such tool requires comparing experimental data with theoretical predictions, where nonintuitive observations present a particular challenge for the theory. Such a challenge is provided by the recent measurements of suppression for charged hadrons [2], unidentified jets [3, 4] and B probes [5, 6] at 2.76 TeV Pb+Pb collisions at the LHC. In particular, in Fig. 1 (the left and the central panels) are shown ATLAS [2, 3] and CMS [4] suppression (R_{AA}) data for different momentum ranges and as a function of both the number of participants (N_{part}), see the left panel, and momentum ($p_\perp$), see the central panel. In particular, ATLAS charged hadron ($h^\pm$) data [2] show that R_{AA} *vs.* N_{part} curves are increasingly flat as one moves towards higher momentum ranges (compare purple, green and blue data points in the left panel). Furthermore, the central panel shows flattening (saturation) of R_{AA} at high momentum, that can be observed for R_{AA} *vs.* $p_\perp$ dependence corresponding to unidentified jets at ATLAS (red squares) [3] and CMS (cyan squares) [4]. These observations are highly nontrivial: the left panel suggest that, while the lower momentum light flavor probes are very sensitive to the N_{part} - and consequently to the system size and energy density- such sensitivity is largely abolished for the high momentum probes. For the central panel, one observes an apparent plateau reached by R_{AA} data at high $p_\perp$, leading to the question what energy loss mechanism is responsible for this effect. Moreover, a qualitatively different R_{AA} *vs.* N_{part} pattern is apparently observed for B mesons: R_{AA} for non-prompt J/Ψ at lower momentum [5] and B jets [6] at high momentum (the purple and the blue dots in the right panel of Fig. 1, respectively), surprisingly show the same R_{AA} *vs.* N_{part} for these two opposite momentum ranges - both of them being largely insensitive to the increase in N_{part}; for observing the difference with $h^\pm$ data, compare the purple and the blue data pints on the left and the right panels of Fig. 1.

We will study the data patterns summarized above within our state-of-the-art dynamical energy loss formalism [7, 8]. Briefly, the formalism takes into account that QGP consists of dynamical (moving) partons - which removes the widely used assumption of static scattering centers - and that the created medium has a finite size. Both collisional [9] and radiative [7, 8] energy losses are calculated within the same theoretical framework, which is applicable to both light and heavy flavor, and includes finite magnetic mass [10] and running coupling [11]. This formalism is integrated in a numerical procedure which takes into account the up-to-date initial distributions [12, 13], fragmentation functions [14], path-length [15, 16] and multi-gluon fluctuations [17]; importantly *no free parameters* are used in comparing the model predictions with the data. Our aim is not only showing that the dynamical energy loss formalism can well explain the complex R_{AA} data patterns, but even more providing an intuitive explanation for the unexpected experimental observations, which may point to an anticipated example of a qualitative interplay between the major energy loss effects. Finally, we will provide predictions for the upcoming experimental measurements that will further test the mechanism proposed here.

Results. The predictions are generated by the dynamical energy loss formalism, where the computational procedure and the parameter set are described in detail in [11]. Briefly, we consider a QGP with $n_f = 3$ and $\Lambda_{QCD} = 0.2$ GeV. For the light quarks, we

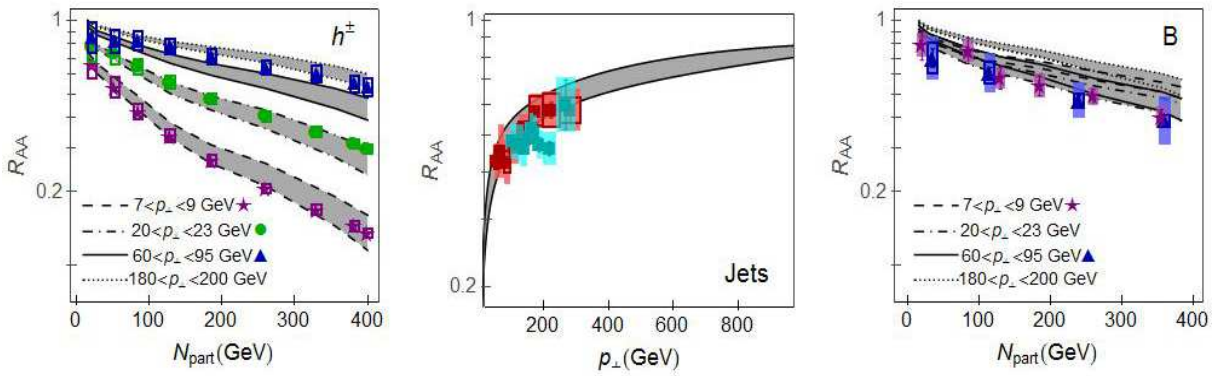

FIG. 1: **Suppression patterns at the LHC.** *Left panel:* Theoretical predictions for R_{AA} *vs.* N_{part} are compared with ATLAS experimental data for $h^{\pm}$ [2], where purple stars, green dots and blue triangles correspond, respectively, to the data for $7 < p_{\perp} < 9$, $20 < p_{\perp} < 23$ and $60 < p_{\perp} < 95$ GeV momentum regions. Gray regions with dashed, dot-dashed, full and dotted bands correspond, respectively, to predictions for $7 < p_{\perp} < 9$, $20 < p_{\perp} < 23$, $60 < p_{\perp} < 95$, $180 < p_{\perp} < 200$ GeV momentum regions. *Central panel:* Theoretical predictions for R_{AA} *vs.* $p_{\perp}$ are compared with ATLAS (red squares) [3] and CMS (cyan squares) [4] most central experimental data for unidentified jets. *Right panel:* Theoretical predictions for R_{AA} *vs.* N_{part} are compared with CMS experimental data for non-prompt J/Ψ (purple stars with $6.5 < p_{\perp} < 30$ GeV) [5] and B jets (blue triangles with $80 < p_{\perp} < 90$ GeV) [6]. The gray regions are equivalent to those in the left panel. On each panel, the upper (lower) boundary of each gray band corresponds to $\mu_M/\mu_E = 0.4$ ($\mu_M/\mu_E = 0.6$).

assume that their mass is dominated by the thermal mass $M = \mu_E/\sqrt{6}$, where the temperature dependent Debye mass $\mu_E(T)$ is obtained from [18]. Magnetic mass μ_M is taken as $0.4\,\mu_E < \mu_M < 0.6\,\mu_E$ [22, 23], the gluon mass is $m_g = \mu_E/\sqrt{2}$ [19] and the bottom mass is $M = 4.75\,\text{GeV}$. Path-length distributions are taken from [16] and temperatures for different centralities from [21]. Note that the same theoretical framework and the parameter set (corresponding to the standard literature values) was previously shown to well agree with the data corresponding to different probes, experiments and centrality regions [11, 20, 21]; consequently, the predictions presented here are well constrained, not only by the absence of the free parameters, but also by the agreement with an extensive set of other data.

In the left panel of Fig. 1, we provide predictions which agree very well with the ATLAS $h^{\pm}$ data [2] for three different momentum ranges ($7 < p_{\perp} < 9$, $20 < p_{\perp} < 23$, $65 < p_{\perp} < 90$ GeV). The predicted curves reproduce well the tendency observed in the data, i.e. as one moves to higher energy ranges, R_{AA} *vs.* N_{part} becomes increasingly flatter. Another tendency of R_{AA} *vs.* N_{part} is also apparent from the predictions, i.e. as one moves towards higher momentum ranges, the difference between the curves becomes increasingly smaller; we will call this the saturation in R_{AA} *vs.* N_{part} curves.

In the central panel of Fig. 1, we see that our predictions are also in an agreement with the measured [3, 4] R_{AA} *vs.* $p_{\perp}$ dependance. Moreover, we see that the "plateau" [3, 4], often referred as surprising, corresponds to the slow increase in the predicted curves, which we further call saturation in R_{AA} *vs.* $p_{\perp}$ dependence. Finally, in the right panel of Fig. 1, we see that our predictions can also well reproduce the experimental data [5, 6] for B probes, which indicate qualitatively substantially different pattern compared to $h^{\pm}$ data. Moreover, the calculated R_{AA} *vs.* N_{part} are largely flat across the *entire* span of the momentum ranges, and the saturation in R_{AA} *vs.* N_{part} curves - which is for light probes observed only at higher $p_{\perp}$ range - is for B probes predicted for the entire momentum span.

The predictions shown in Fig. 1 contain several features, similar to those indicated by the experimental data (see the Introduction). First, the flattening and the saturation observed in R_{AA} *vs.* N_{part} curves for $h^{\pm}$ indicate that, at high $p_{\perp}$, the predictions are largely insensitive to the collision centrality, and consequently to the corresponding changes in the medium properties; this is in contrast to the lower $p_{\perp}$, where predictions exhibit a considerable sensitivity to the collision centrality. Furthermore, the saturation observed in R_{AA} *vs.* $p_{\perp}$ predictions - consistent with the corresponding plateau in the experimental data - indicates an unexpectedly slow change of jet energy loss with the initial jet energy at high $p_{\perp}$. Finally, the R_{AA} *vs.* N_{part} pattern predicted for the B probes is also surprising: here, a qualitatively different pattern compared to the light probes is obtained, where B probes are now largely insensitive to the medium properties across the entire momentum span - as opposed to the $h^{\pm}$ insensitivity at only high $p_{\perp}$. As the available data for B probes indicated in the right panel are limited (and indirect, i.e. corresponding to the different observables), note that the calculated B meson results also correspond to novel predictions, whose comparison with the upcoming data will test how our formalism can explain qualitatively unexpected observations.

We therefore aim understanding the nonintuitive patterns in the predictions/data outlined above. For the light probes, this explanation is provided by the upper left panel of Fig. 2, which shows R_{AA} *vs.* $p_\perp$ dependence for a family of curves corresponding to increasing collision centrality. Note two main properties of these curves: First, their shape, which leads to the saturation in R_{AA} *vs.* $p_\perp$ exhibited in the central panel in Fig. 1; this property will be explained by the upper central and the right panels in Fig. 2. Secondly, their density, which (non-uniformly) increases as one moves from lower to high $p_\perp$ - with that respect, it may be useful to observe R_{AA} *vs.* $p_\perp$ curves as field flux lines. For visualizing how the relevant curve density changes, three vertical arrows are indicated in the upper left panel of Fig. 2 - these arrows relate to understanding $h^\pm$ R_{AA} *vs.* N_{part} predictions in the left panel of Fig. 1. Specifically, the leftmost arrow, corresponding to lower ($\sim$ 10 GeV) $p_\perp$, spans a much larger R_{AA} range compared to the two right arrows, which correspond to higher $p_\perp$. This observation directly translates to the fact that R_{AA} *vs.* N_{part} curves are much steeper at lower, compared to high, $p_\perp$ ranges. Moreover, there is a much larger difference in R_{AA} span between the leftmost and the central arrows, as compared to the central and the rightmost arrows; this being despite the fact that the three arrows are spaced equidistantly in momentum. A direct consequence of these differences in R_{AA} span, is the saturation in R_{AA} *vs.* N_{part} in the left panel of Fig. 1, i.e. the fact that there is an increasingly smaller difference between R_{AA} *vs.* N_{part} curves as one moves towards increasingly higher momentum ranges.

The shape of the total R_{AA} *vs.* $p_\perp$ curves (leading to the saturation in the central panel of Fig. 1) is a consequence of an interplay between the collisional and the radiative contributions to the suppression. As can be seen at the upper central panel of Fig. 2, the collisional contribution to the R_{AA} is notable for smaller $p_\perp$, where it increases steeply with momentum, rapidly approaching 1 at high $p_\perp$, providing a small contribution to total R_{AA} at high $p_\perp$ region. On the other hand, the radiative contribution increases much slower with the momentum, and has a significant contribution to R_{AA} even at higher $p_\perp$. Consequently, the steep increase in total R_{AA} at lower $p_\perp$ is driven by the dominant collisional contribution to R_{AA} in that momentum range, while the slow increase (apparent saturation) of R_{AA} at high $p_\perp$ is due to the dominant radiative contribution. This interplay then explains the saturation (plateau) of R_{AA} observed at high $p_\perp$. Moreover, such interplay between the collisional and the radiative contributions to R_{AA}, also determines the density of R_{AA} *vs.* $p_\perp$ curves. As can be seen from the vertical arrows indicated in the upper central and the right panels in Fig. 2, the collisional contribution is responsible for the large span of total R_{AA} with changing centrality at lower momentum. On the other hand, at higher momentum, the radiative contribution exhibits a significantly smaller and largely uniform R_{AA} span, therefore resulting in the larger and more uniform total R_{AA} curve density in that momentum range.

An intuitive explanation behind the different R_{AA} *vs.* N_{part} pattern observed for B probes (the right panel in Fig. 1) is provided by the lower panels of Fig. 2. In distinction to $h^\pm$, in the lower left panel, we see that total R_{AA} *vs.* $p_\perp$ curves have mostly uniform density, with a largely flat shape of the curves across the entire momentum range. The difference with respect to $h^\pm$ is clearly due to the radiative contribution to the total R_{AA}, as the curves corresponding to the B meson collisional contribution are largely equivalent to those for $h^\pm$ (compare the upper and lower central panels in Fig.2). In particular, note an unusual shape of radiative R_{AA} *vs.* $p_\perp$ curves (the lower right panel), which is a consequence of a strong dead-cone effect [24] in bottom quark energy loss. This unusual shape leads to a large density of radiative R_{AA} *vs.* $p_\perp$ curves at lower momentum, and to a largely uniform curve density for high momentum. As a consequence, for lower momentum, the effect of the relatively large R_{AA} span for the collisional contribution is abolished by the small R_{AA} span for the radiative contribution, this leading to the flat and uniform density for total R_{AA} *vs.* $p_\perp$ curves observed in the lower left panel of Fig.2. Such curve shape then evidently leads to a largely uniform total R_{AA} span across the whole range of momentum, as indicated by the three vertical arrows in the lower left panel of Fig.2, which then leads to the largely flat and almost overlapping R_{AA} *vs.* N_{part} curves for B mesons, as observed in the right panel of Fig. 1.

Conclusion. A starting point for this work is an observation of a plateau reached at high momentum for R_{AA} *vs.* $p_\perp$ measurements. Starting from this observation, we here combined related experimental data, which reveal an unexpected pattern in the R_{AA} data. We showed that these data patterns are well reproduced by the theoretical predictions for charged hadrons and unidentified jets, with no free parameters used. For B mesons, we predict that the tendency indicated by the limited available data will be exhibited across the entire span of the momentum ranges - this prediction will be tested in the future.

We showed that these complex data patterns have, in fact, a simple qualitative interpretation, where it is useful to observe R_{AA} *vs.* $p_\perp$ curves as field flux lines whose density changes across different momentum. These curve properties - which lead to the unexpected dependence of R_{AA} on N_{part} and $p_\perp$, and to qualitatively different R_{AA} patterns for the light and heavy probes - are determined by an interplay of collisional, radiative energy loss and the dead-cone effect.

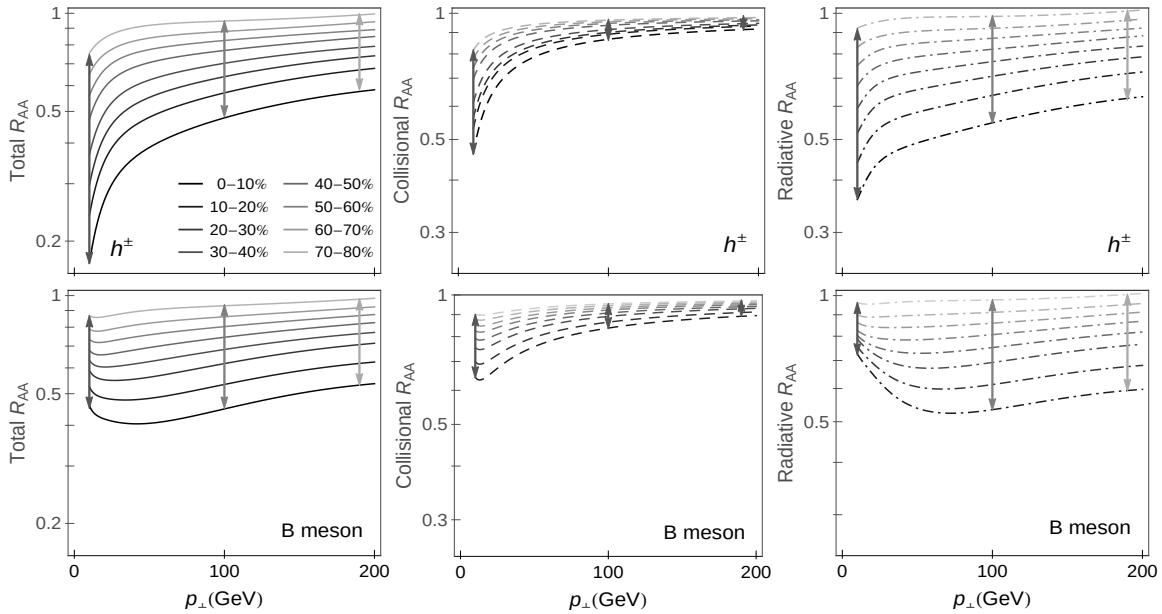

FIG. 2: R_{AA} *vs.* $p_{\perp}$ **for different centrality regions.** Left, central and right panels show, respectively, total, collisional and radiative contributions to R_{AA}. Upper and lower panels correspond to $h^{\pm}$ and B mesons, respectively. On each panel, different curves correspond to different centrality regions, as denoted by the legend in the upper left panel (μ_M/μ_E is set to 0.4). Also, on each panel, three double-sided arrows represent the R_{AA} spans for, respectively, $p_{\perp}$ of 10, 100 and 190 GeV.

Consequently, the results presented here provide a rare opportunity to qualitatively assess how the theory can account for two crucial effects: First, different suppression patterns exhibited by different probe types (here B mesons vs. charged hadrons), providing a clear test of the dead cone effect. Second, contributions of different energy loss mechanisms, providing a test of an interplay between the collisional and the radiative energy loss. This point is even more important having in mind extensive experimental efforts aimed at assessing contributions of various energy loss effects. Consequently, this study provides both an important test of explaining and predicting complex data patterns and a clear qualitative example for distinguishing between major energy loss mechanisms.

Acknowledgments: This work is supported by Marie Curie IRG within the 7^{th} EC Framework Programme (PIRG08-GA-2010-276913) and by the Ministry of Science of the Republic of Serbia under project No. ON173052. I thank B. Blagojevic for help with numerics and Marko Djordjevic for useful discussions.

[1] J.D. Bjorken: FERMILAB-PUB-82V059-THY (1982) 287, 292
[2] **ATLAS** Collaboration, G. Aad *et al.*, JHEP **09**, 050 (2015).
[3] **ATLAS** Collaboration, G. Aad *et al.*, Phys. Rev. Lett. **114** 072302 (2015).
[4] G.I. Veres (for **CMS** Collaboration) Nucl. Phys. A **904905**, 146c153c (2013).
[5] **CMS** Collaboration, S. Chatrchyan *et al.*, JHEP **5**, 063 (2012).
[6] **CMS** Collaboration, S. Chatrchyan *et al.*, Phys. Rev. Lett. **113**, 132301 (2014).
[7] M. Djordjevic, Phys. Rev. C **80**, 064909 (2009).
[8] M. Djordjevic and U. Heinz, Phys. Rev. Lett. **101**, 022302 (2008).
[9] M. Djordjevic, Phys. Rev. C **74**, 064907 (2006).
[10] M. Djordjevic, Phys. Lett. B **709**, 229 (2012)
[11] M. Djordjevic and M. Djordjevic, Phys. Lett. B **734**, 286 (2014).
[12] M. Cacciari, S. Frixione, N. Houdeau, M. L. Mangano, P. Nason and G. Ridolfi, JHEP **1210**, 137 (2012)
[13] Z.B. Kang, I. Vitev and H. Xing, Phys. Lett. B **718**, 482 (2012), R. Sharma, I. Vitev and B.W. Zhang, Phys. Rev. C **80**, 054902 (2009)
[14] D. de Florian, R. Sassot and M. Stratmann, Phys. Rev. D **75**, 114010 (2007).
[15] S. Wicks, W. Horowitz, M. Djordjevic and M. Gyulassy, Nucl. Phys. A **784**, 426 (2007).
[16] A. Dainese, Eur. Phys. J. C **33**, 495 (2004).
[17] M. Gyulassy, P. Levai and I. Vitev, Phys. Lett. B **538**, 282 (2002).
[18] A. Peshier, hep-ph/0601119 (2006).
[19] M. Djordjevic and M. Gyulassy, Phys. Rev. C **68**, 034914 (2003).
[20] M. Djordjevic, Phys. Rev. Lett. **734**, 286 (2014).
[21] M. Djordjevic, M. Djordjevic and B. Blagojevic, Phys. Lett. B **737**, 298 (2014).
[22] Yu. Maezawa *et al.* [WHOT-QCD Collaboration], Phys. Rev. D **81** 091501 (2010);
[23] A. Nakamura, T. Saito and S. Sakai, Phys. Rev. D **69**, 014506 (2004).
[24] Yu. L. Dokshitzer and D. Kharzeev, Phys. Lett. B **519**, 199 (2001).